Electronic Supplementary Material (ESI) for Chemical Science.

Supporting information for

H-bond Stabilized Quinone Electrode Material for Li-Organic Batteries: the Strength of Weak Bonds

Louis Sieuw,[†] Alia Jouhara,[‡] Éric Quarez,[‡] Chloé Auger,[‡] Jean-François Gohy,[†] Philippe Poizot,[‡,*] and Alexandru Vlad[†,*]

[†] Institute de la Matière Condense et des Nanosciences (IMCN), Université catholique de Louvain, Place L. Pasteur 1, 1348 Louvain-la-Neuve, Belgium.

[‡] Institut des Matériaux Jean Rouxel (IMN), UMR CNRS 6502, Université de Nantes, 2 rue de la Houssinière, B.P. 32229, 44322 Nantes Cedex 3, France.

Supporting Online Material:

Figure S1.

Synthesis and characterization: (A) synthesis scheme of DABQ; (B) ^{1}H NMR spectrum of DABQ (C) optical photograph of synthesized DABQ powder; (D) FTIR spectrum of DABQ.

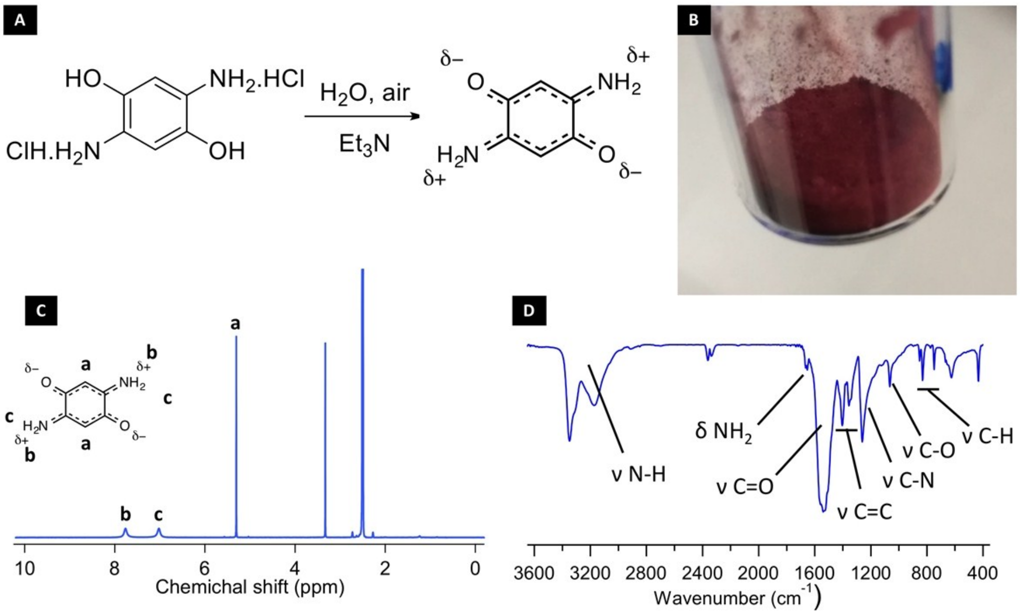

DABQ was synthesized through the oxidation of the corresponding hydroquinone in air (no additional oxidizing agent was used). The pure product was retrieved as a purple powder, characterized by ^{1}H NMR (300 MHz) measured in DMSO and FTIR analysis (KBr pellet).

Figure S2.
Illustration of parallel and perpendicular layers with connecting H-bonds in DABQ.

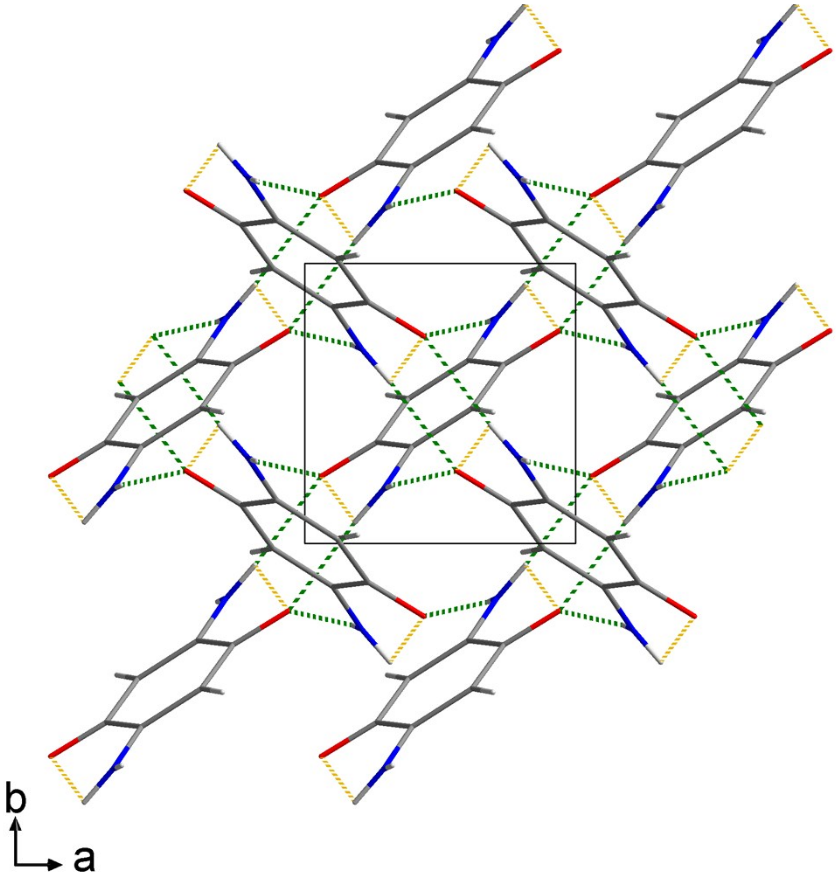

The crystal structure of DABQ was determined from its PXRD diffractogram (ESRF, Grenoble) using Fox ('Free Objects for Crystallography') to find a structure solution and JANA2006 to refine the structure. The individual molecules assemble into layers that stack in a parallel manner with adjacent layers being perpendicular to each other. Intramolecular and intermolecular H-bonding is observed between the polarized amino and carbonyl groups.

Table 1.

Powder Data, Data Collection and Structure Refinement Parameters for $C_6H_6N_2O_2$

formula	$C_6H_6N_2O_2$
Powder Data	
temperature (K)	295
M_r	138.1
crystal symmetry	Monoclinic
space group	$P2_1/n$
a (Å)	5.2532 (4)
b (Å)	5.3210 (3)
c (Å)	10.9671 (7)
β (deg.)	101.9740 (17)°
V (Å^3)	299.88 (4)
Z	2
D_x (g cm^{-3})	1.530
Data Collection	
λ (Å)	0.7458
θ_{min}–θ_{max} (deg.)	2.52–41.39
2θ step (deg.)	0.01
Refinement	
Profile function	Pseudo-Voigt
R_p	0.011
R_{wp}	0.020
R_{exp}	0.001
$R(F)$	0.067
$(\Delta/\sigma)_{max}$	0.007

Table 2.

Fractional atomic coordinates and isotropic displacement parameters (Å^2) for $C_6H_6N_2O_2$

	x	*y*	*z*	U_{iso}
C1	0.7345 (7)	0.6385 (7)	0.5557 (2)	0.0095 (9)
C2	0.6036 (7)	0.6539 (7)	0.41723 (18)	0.0095 (9)
C3	0.6178 (7)	0.4827 (6)	0.6292 (3)	0.0095 (9)
N1	0.7102 (8)	0.8061 (7)	0.35128 (19)	0.0263 (13)
O1	0.9392 (5)	0.7595 (4)	0.5889 (2)	0.0262 (10)
H1	0.677482	0.79196	0.270498	0.0315
H2	0.814793	0.923131	0.387532	0.0315
H3	0.694696	0.469265	0.716383	0.0114

Table 3.

Geometric parameters (Å, °) for $C_6H_6N_2O_2$

C1—C2	1.534 (3)	C2—N1	1.289 (5)
C1—C3	1.385 (5)	C3—H3	0.96
C1—O1	1.241 (4)	N1—H1	0.87
C2—C3$^{\text{i}}$	1.376 (5)	N1—H2	0.87
C2—C1—C3	116.5 (3)	C1—C3—C2$^{\text{i}}$	122.9 (3)
C2—C1—O1	116.4 (3)	C1—C3—H3	118.57
C3—C1—O1	127.0 (3)	C2$^{\text{i}}$—C3—H3	118.57
C1—C2—C3$^{\text{i}}$	120.6 (3)	C2—N1—H1	120
C1—C2—N1	115.6 (3)	C2—N1—H2	120
C3$^{\text{i}}$—C2—N1	123.8 (3)	H1—N1—H2	120

Symmetry code: (i) $-x+1$, $-y+1$, $-z+1$.

Table 4.

Hydrogen-bond geometry (Å, °) for $C_6H_6N_2O_2$

D—H···*A*	*D*—H	H···*A*	*D*···*A*	*D*—H···*A*
N1—H1···O1$^{\text{ii}}$	0.87	2.14	2.955 (3)	155.95
N1—H2···O1	0.87	2.34	2.645 (3)	101.04
N1—H2···O1$^{\text{iii}}$	0.87	2.11	2.943 (4)	160.33

Symmetry codes: (ii) $x-1/2$, $-y+3/2$, $z-1/2$; (iii) $-x+2$, $-y+2$, $-z+1$.

Figure S3.

SEM image based on the collect of backscattered electrons (BSE) obtained at 5 kV revealing the lamellar morphology of DABQ particles.

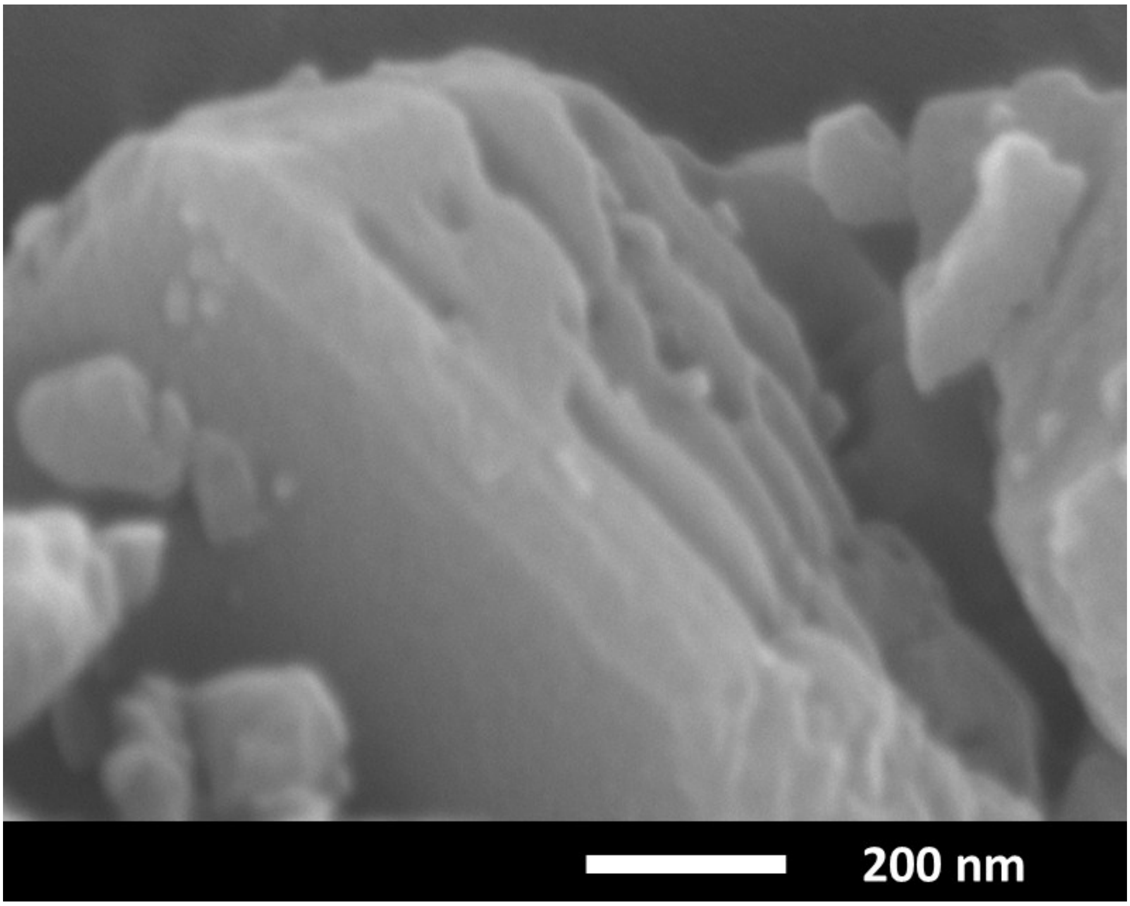

Figure S4.

N-substituted alkyl DABQ derivatives: *N*,*N'*-dimethyl-2,5-diaminobenzoquinone (DMDABQ) and *N*,*N'*-diethyl-2,5-diaminobenzoquinone (DEDABQ) compared to DABQ: (A) molecular structure, (B) qualitative solubility (optical photographs) and (C) galvanostatic cycling.

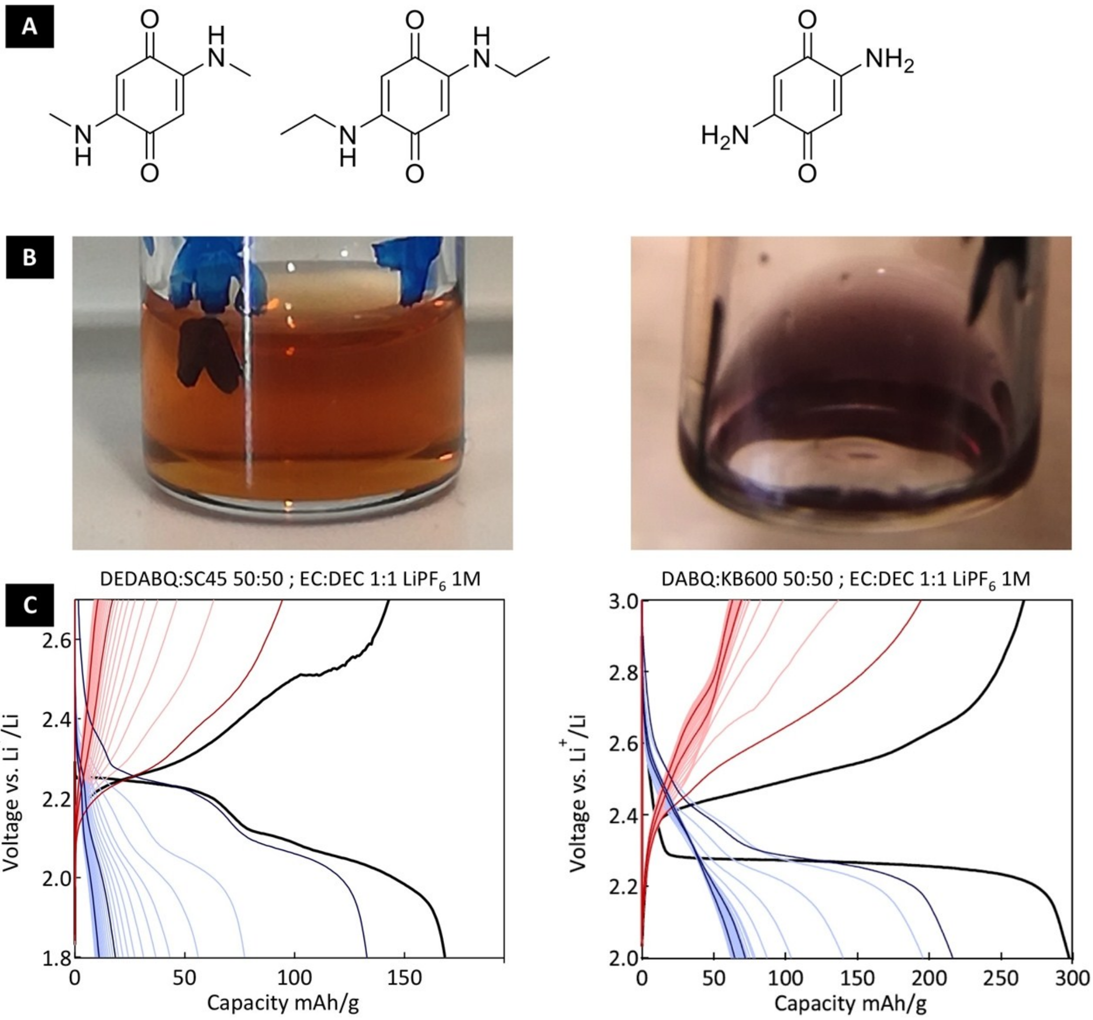

Introducing alkyl chains on the N atom disturbed the H-bonding of DABQ, hence elevated solubility and poorer cycling stabilities in battery electrolytes.

Figure S5.

(A) DABQ UV-Vis absorption spectrum; and (B) solubility calibration plot.

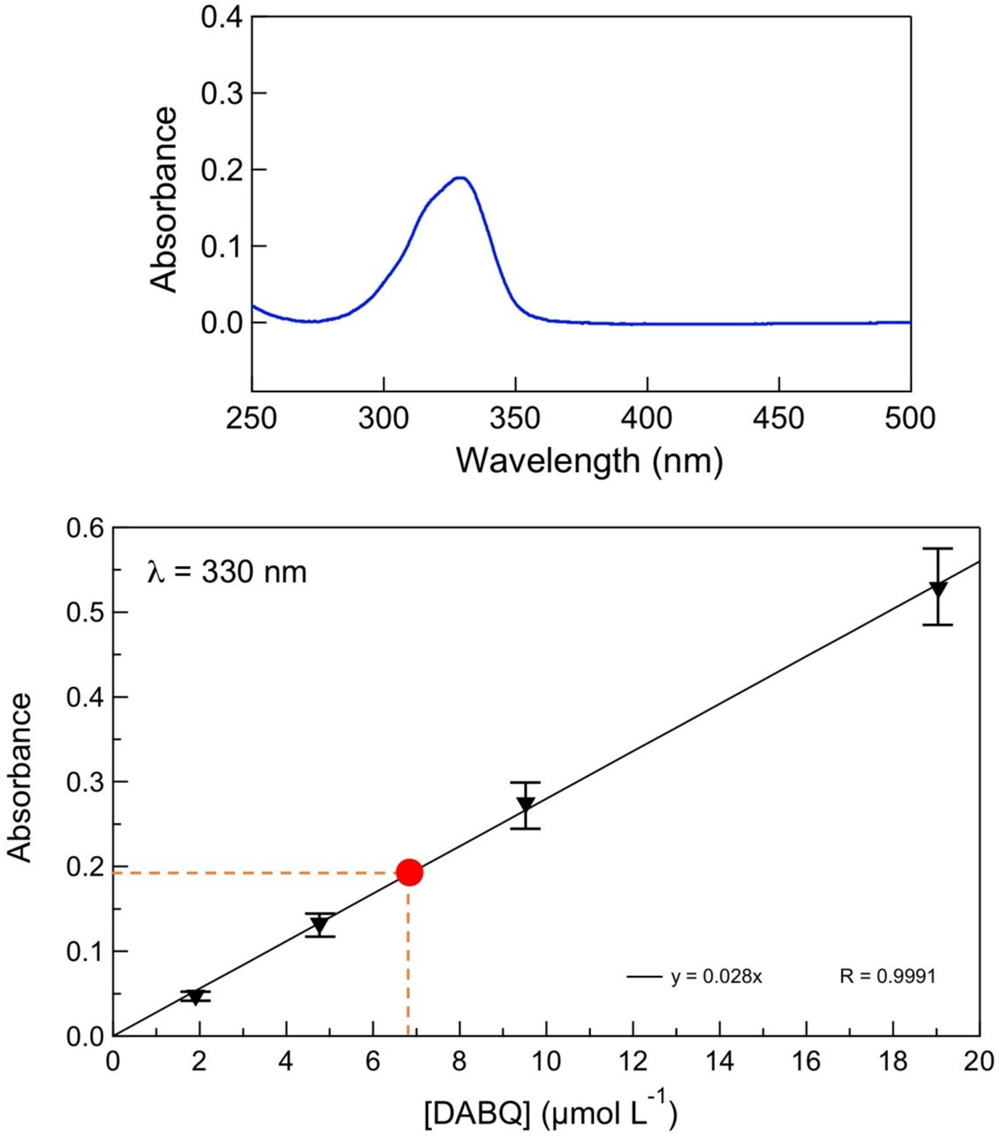

UV-Visible spectra were recorded using a Shimadzu UV-1700 PharmaSpec (Fig. S1). Samples were analyzed in quartz cuvettes. Saturated solutions of DABQ were prepared by adding 2 mg of the powder in 3 mL electrolyte. The resulting mixture was filtered through Millipore Millex-HV PVDF 0.45 µm filters to remove the excess insolubilized DABQ. The saturated solution was subsequently diluted by a factor 100.

Standard solutions were prepared in the number of four for each electrolyte with DABQ concentrations of 2, 5, 10 and 20µM. Absorbance was measured in the 200-800 nm range for all solutions. The calibration curve was obtained by linking the maximum absorbance (330 nm) of the standard solutions to their concentrations in DABQ using the Beer-Lambert law: $A=\varepsilon lC$ (A: absorbance; ε: molar extinction coefficient; l: length of the cell; C: DABQ concentration).

Figure S6.

Galvanostatic cycling of DABQ in DMC LiTFSI 1M: potential-composition traces for the five first cycles.

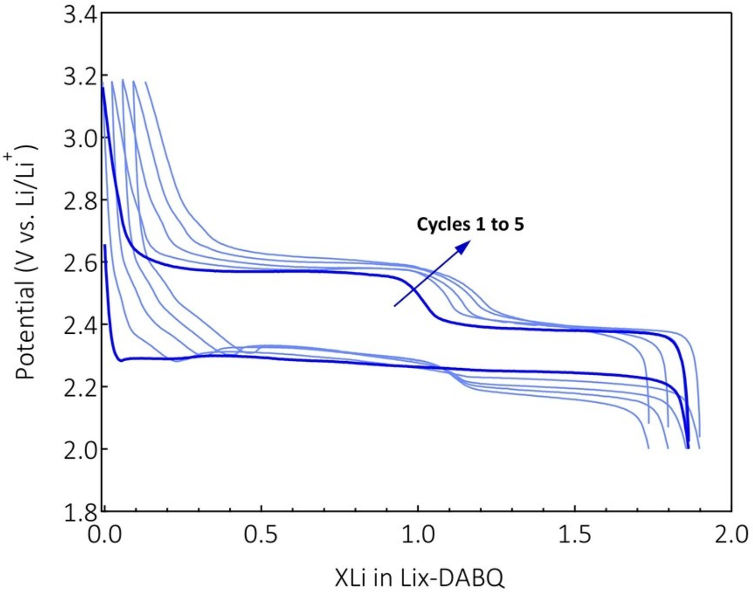

Having the lowest dipole moment of the electrolyte solvents tested, DMC (μ=0.76 D) allowed to decrease the solubility of DABQ to 65 mg/L. This led to cycling performances similar to those in ether electrolytes.

Figure S7.

Post cycling analysis: (A) SEM surface images of pristine and cycled DABQ electrodes. Holes in the carbon/binder layer are visible corresponding to the dissolution of DABQ crystals. (B) optical photographs of electrode, PE/PP separator and lithium chip after cycling in carbonate electrolyte.

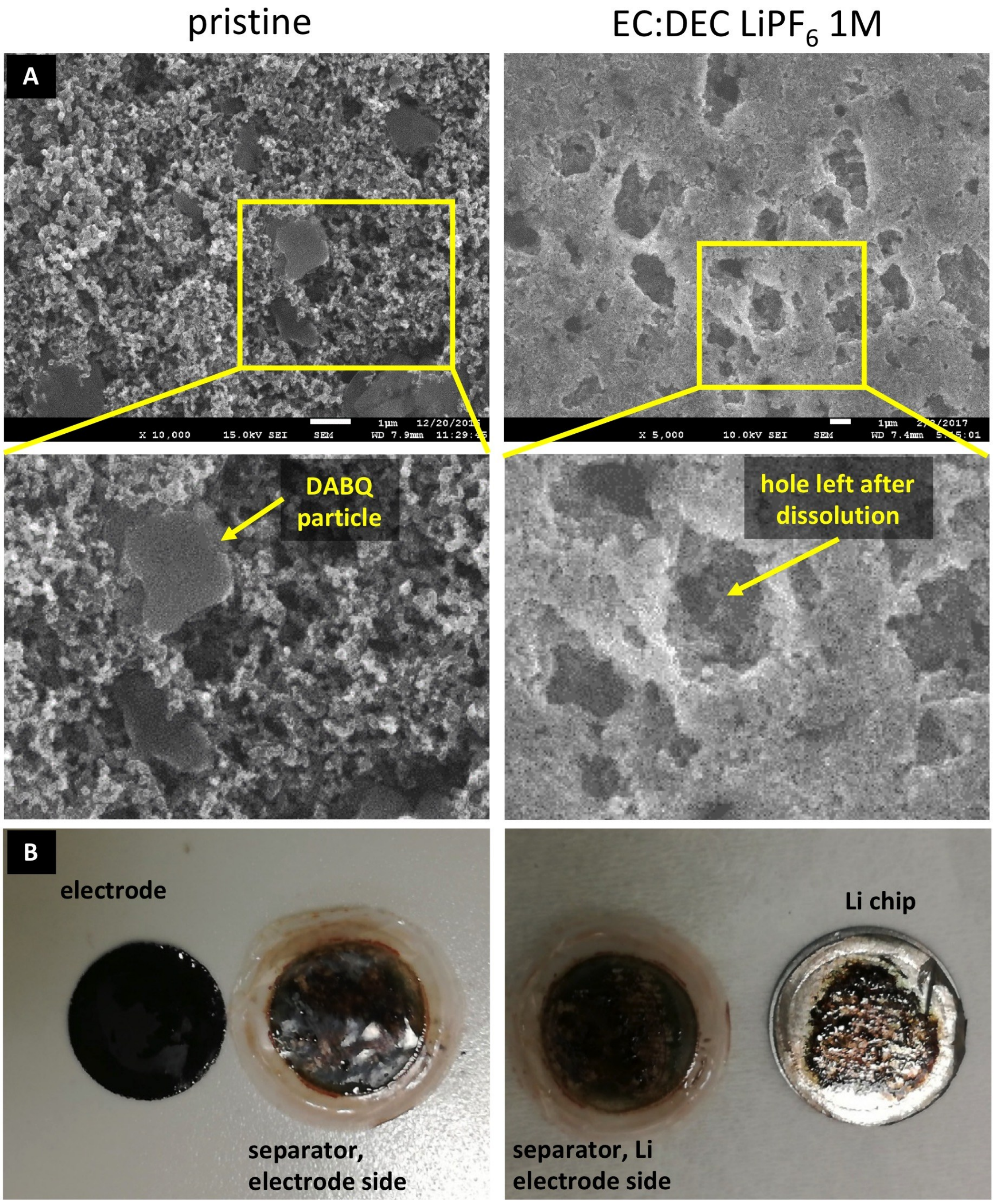

Galvanostatic cycling of DABQ in carbonate electrolytes resulted in important capacity loss. SEM analysis of the electrode (DABQ:KB600:PVDF 60:30:10) before and after cycling revealed the loss of DABQ crystals in the carbon network, following the dissolution of the active material in the electrolyte during cycling (Fig. S6A). Moreover, upon inspection of the other cell constituents, we observed a purple coloration of the separator and Li electrode. This is ascribed to DABQ being solubilized by the electrolyte and deposited on these cell elements.

Figure S8.

Cycling stability in TEGDME/DOL electrolytes using 0.25, 1 and 2 M LiTFSI, respectively.

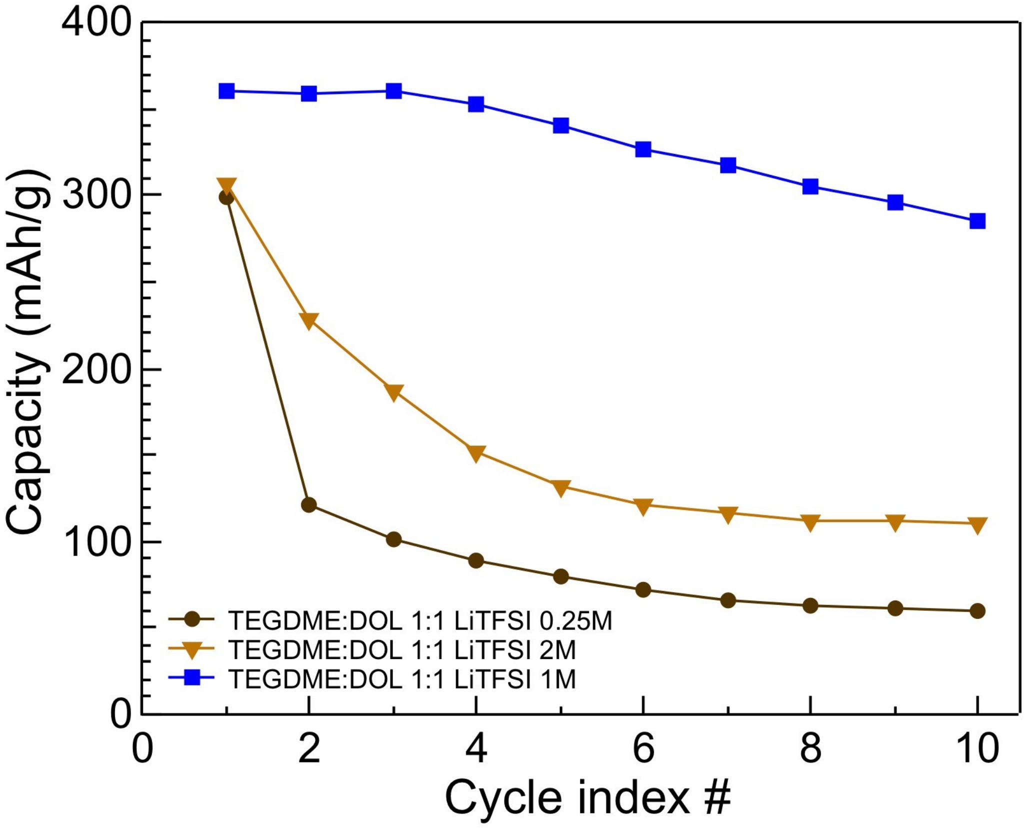

Increasing the LITFSI content from 1 M to 2 M leads to a considerable solubility increase that is translated into a much lower first cycle efficiency and consequently quicker loss of capacity with cycling. Conversely, while an electrolyte with only 0.25 M LiTFSI slightly reduces the solubility, the electrochemical cycling stability and efficiency are considerably worse. This is ascribed to the ionic conductivity of the electrolyte, rendered insufficient by the decrease in electrolyte salt concentration.

Figure S9.

BQ vs DABQ electrochemical cycling. The residual capacity for the BQ cell is due to the double layer charge storage in the used Ketjenblack EC600JD carbon black.

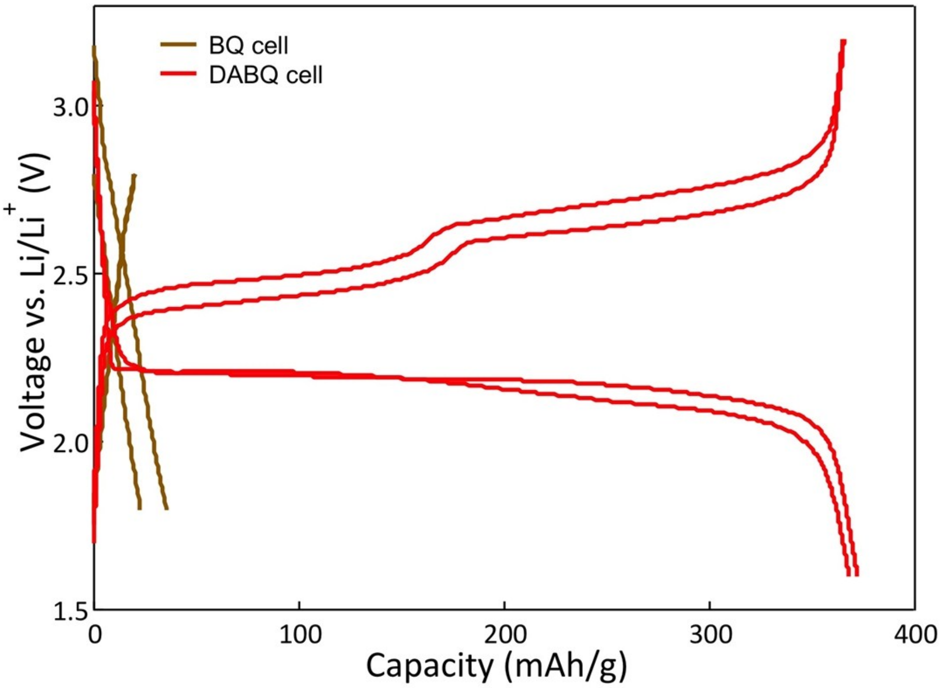

Due to its very high solubility in organic electrolytes (200 g/L measured here), galvanostatic cycling of BQ in the solid state does not allow to observe any redox process. Indeed, only a small capacitive response from the carbon additive is obtained, compared to the full 2-electron process of DABQ in the same electrolyte (EC/DEC $LiPF_6$ 1 M).